APPLIED MATHEMATICS AND MECHANICS (ENGLISH EDITION)

Nonlinear dynamic responses of sandwich functionally graded porous cylindrical shells embedded in elastic media under 1:1 internal resonance*

Yunfei LIU,   Zhaoye QIN†,   Fulei CHU

State Key Laboratory of Tribology, Department of Mechanical Engineering,

Tsinghua University, Beijing 100084, China

(Received Jan. 17, 2021 / Revised Mar. 18, 2021)

Abstract   In this article, the nonlinear dynamic responses of sandwich functionally graded (FG) porous cylindrical shell embedded in elastic media are investigated. The shell studied here consists of three layers, of which the outer and inner skins are made of solid metal, while the core is FG porous metal foam. Partial differential equations are derived by utilizing the improved Donnell's nonlinear shell theory and Hamilton's principle. Afterwards, the Galerkin method is used to transform the governing equations into nonlinear ordinary differential equations, and an approximate analytical solution is obtained by using the multiple scales method. The effects of various system parameters, specifically, the radial load, core thickness, foam type, foam coefficient, structure damping, and Winkler-Pasternak foundation parameters on nonlinear internal resonance of the sandwich FG porous thin shells are evaluated.

Key words   nonlinear internal resonance, sandwich functionally graded (FG) porous shell, improved Donnell's nonlinear shell theory, multiple scales method, Galerkin method

Chinese Library Classification   O322
2010 Mathematics Subject Classification   74H45

1   Introduction

Compared with ordinary metal materials, the metal foam has many voids within the material, which results in notable physical and mechanical features involving low weight and high specific surface area, good impact energy absorption, excellent noise attenuation, high thermal conductivity combined with high gas permeability, machinability, and weld ability. Based on these excellent properties, the porous metal foam structure has been widely employed in various engineering applications, such as tissue engineering[1], shock absorbers[2], energy absorbers[3], porous electrodes[4], and produce filters[5], which is becoming a kind of multifunctional engineering structure[6].

In practical engineering applications, those metal foam structures are commonly subjected to severe dynamic loads, and prone to unexpected nonlinear vibrations and complex internal resonances, which may affect their normal operation or even damage the structures. The occurrence of nonlinear internal resonances could lead to large amplitude vibrations, irrecoverable deformations, noises, cracks, and even the failure of structures. Therefore, knowledge and prediction of resonant characteristics of porous metal foam structures are essential for their reliability and security.

Thin shell configurations are commonly employed under various dynamic loading conditions; for instance, they can serve as key components for aircraft, rocket propulsion systems, and large deployable space loop antennas. Thus, understanding the nonlinear internal resonant behaviors of thin cylindrical shells, to ensure their reliability, is critical. Therefore, some theoretical studies have been carried out to clarify the internal resonance of thin shells. Breslavsky and Amabili[7] studied the multiple internal resonances of thin cylindrical shells under multiharmonic excitation. Under the non-normal boundary condition, the $1:2$ internal resonance of thin shells was investigated by Yang et al.[8]. Zhang et al.[9] carried out a study on the nonlinear resonant response of rotary thin shells. Considering the influence of initial geometric imperfections, Rodrigues et al.[10] examined the $1:1:1:1$ internal resonant behavior of thin cylindrical shells.

Despite the necessity of comprehensive understanding of nonlinear resonant response, up to now, only the linear responses of functionally graded (FG) porous structures have been reported in a few references. Liu et al.[11] gave an analytical solution to the impact response of sandwich FG porous shells. Dong et al.[12] studied the linear vibration of graphene platelet reinforced FG porous metal foam shells with spinning motion. The dynamic stability of graphene platelet reinforced sandwich porous plates via the classical plate theory was studied by Li et al.[13]. Chen et al.[14] considered two different porosity distributions to study the free and forced vibrations of porous metal foam beams. The wave propagation in graphene platelet reinforced FG porous metal foam plates was studied by Gao et al.[15]. Liu and Wang[16] investigated the thermo-electro-mechanical vibrations of porous piezoelectric nanoshells.

Literature review shows that no study has been reported on nonlinear internal resonance analysis of sandwich FG porous thin cylindrical shells. Therefore, the present work attempts to provide a solution approach for this issue and investigate $1:1$ internal resonant response of sandwich FG porous thin shells. The dynamic model is established by using the improved Donnell's nonlinear shell theory. Hamilton's principle is used to derive the governing equations. Afterwards, the nonlinear solutions are discretized by the Galerkin method. The multiple scales method is used to obtain an approximate analytical solution to the multi-degree-of-freedom systems. Finally, discussion is presented to carry out the nonlinear dynamic analysis and parametric study for the sandwich FG porous shells' nonlinear internal resonance.

2 Theoretical formulation

As shown in Fig. 1, considering an embedded sandwich FG porous thin shell with thickness h, length L, and radius R, the outer and inner layers are pure metal, and the core is FG porous metal foam. It is assumed that the porous core and surface layers are perfectly bonded. The elastic media are characterized by the Winkler-Pasternak foundation model, where the Winkler and Pasternak foundation parameters are k_w and k_p, respectively. The shell is subjected to a harmonic point excitation in the radial direction. The displacement components of points at the shell mid-plane are denoted by u, v, and w in the x-, θ-, and z-directions, respectively.

As seen in Fig. 2, three types of porous metal foam distributions are considered for the FG porous core as porous metal foam-I, porous metal foam-II, and porous metal foam-III. Varying material properties of three metal foam distribution types are given as follows[17–19]:
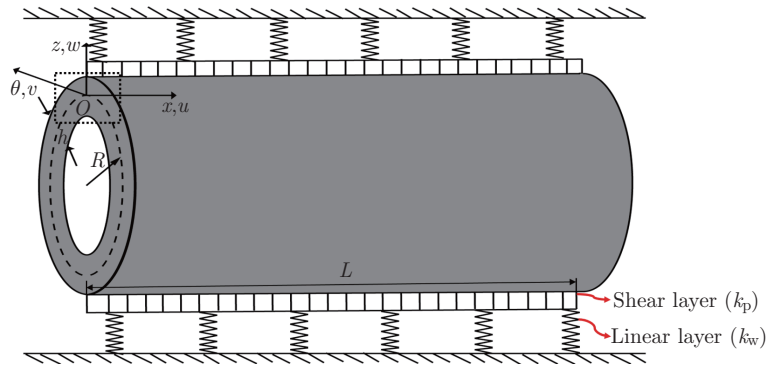
Fig. 1 Schematic of embedded sandwich FG porous thin shell

(a) Porous metal foam-I

(b) Porous metal foam-II
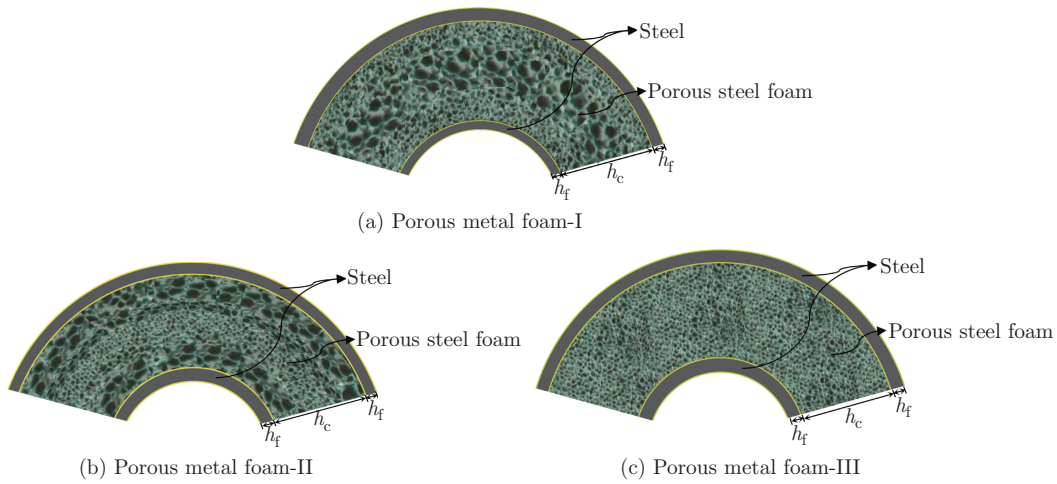
(c) Porous metal foam-III

Fig. 2 Distribution types of porosity: (a) porous metal foam-I, (b) porous metal foam-II, and (c) porous metal foam-III (color online)

Porous metal foam-I,

$$\rho(z) = \rho_1 \Big(1 - \zeta_{\mathrm{m}} \cos \Big(\frac{\pi z}{h_{\mathrm{c}}} \Big) \Big), \tag{1}$$

$$E(z) = E_1 \Big(1 - \zeta_0 \cos \Big(\frac{\pi z}{h_{\mathrm{c}}} \Big) \Big), \tag{2}$$

$$G(z) = G_1 \Big(1 - \zeta_0 \cos \Big(\frac{\pi z}{h_{\mathrm{c}}} \Big) \Big). \tag{3}$$

Porous metal foam-II,

$$\rho(z) = \rho_1 \Big(1 - \zeta_{\mathrm{m}}^* \Big(1 - \cos \Big(\frac{\pi z}{h_{\mathrm{c}}} \Big) \Big) \Big), \tag{4}$$

$$E(z) = E_1 \Big(1 - \zeta_0^* \Big(1 - \cos \Big(\frac{\pi z}{h_{\mathrm{c}}} \Big) \Big) \Big), \tag{5}$$

$$G(z) = G_1 \Big(1 - \zeta_0^* \Big(1 - \cos \Big(\frac{\pi z}{h_{\mathrm{c}}} \Big) \Big) \Big). \tag{6}$$

Porous metal foam-III,

$$\rho(z) = \rho_1 \vartheta', \tag{7}$$

$$E(z) = E_1 \vartheta, \tag{8}$$

$$G(z) = G_1 \vartheta. \tag{9}$$

Here, ρ_1, E_1, and G_1 denote the mass density, Young's modules, and shear modules of pure steel, respectively, $\zeta_{\mathrm{m}}, \zeta_{\mathrm{m}}^*$, and ϑ' represent coefficients of mass density for porous metal foam-I, porous metal foam-II, and porous metal foam-III, respectively, and ζ_0, ζ_0^*, and ϑ are foam coefficients of the corresponding porous metal foam distributions, respectively.

The relation between E and ρ, for open-cell metal foams, is given by[14,17,20]

$$\frac{E(z)}{E_1} = \left(\frac{\rho(z)}{\rho_1}\right)^2. \tag{10}$$

The relations between foam and mass density coefficients are expressed as

$$\begin{cases} 1 - \zeta_{\mathrm{m}} \cos\left(\frac{\pi z}{h}\right) = \sqrt{1 - \zeta_0 \cos\left(\frac{\pi z}{h}\right)} & \text{for porous metal foam-I}, \\ 1 - \zeta_{\mathrm{m}}^* \left(1 - \cos\left(\frac{\pi z}{h}\right)\right) = \sqrt{1 - \zeta_0^* \left(1 - \cos\left(\frac{\pi z}{h}\right)\right)} & \text{for porous metal foam-II}, \\ \vartheta' = \sqrt{\vartheta} & \text{for porous metal foam-III}. \end{cases} \tag{11}$$

Assume that the masses of all types of porous core are equivalent, namely,

$$\begin{cases} \int_0^{h_c/2} \sqrt{1 - \zeta_0^* \left(1 - \cos\left(\frac{\pi z}{h}\right)\right)} \mathrm{d}z = \int_0^{h_c/2} \sqrt{1 - \zeta_0 \cos\left(\frac{\pi z}{h}\right)} \mathrm{d}z, \\ \int_0^{h_c/2} \sqrt{\vartheta} \mathrm{d}z = \int_0^{h_c/2} \sqrt{1 - \zeta_0 \cos\left(\frac{\pi z}{h}\right)} \mathrm{d}z. \end{cases} \tag{12}$$

By using Eq. (12), ζ_0^* and ϑ can be determined with a given ζ_0.

The strain components at an arbitrary point of the embedded sandwich FG porous thin shell could be written as[21]

$$\begin{pmatrix} \varepsilon_{xx} \\ \varepsilon_{\theta\theta} \\ \gamma_{x\theta} \end{pmatrix} = \begin{pmatrix} \varepsilon_x^0 \\ \varepsilon_\theta^0 \\ \gamma_{x\theta}^0 \end{pmatrix} + z \begin{pmatrix} k_x \\ k_\theta \\ 2k_{x\theta} \end{pmatrix}, \tag{13}$$

in which ε_x^0, ε_θ^0, and $\gamma_{x\theta}^0$ define the strains of the middle surface; k_x, k_θ, and $k_{x\theta}$ are the middle-surface curvature and torsion, respectively.

To overcome the inaccuracy of Donnell's nonlinear shell theory at small circumferential wave number, the nonlinear strain-displacement relations, based on the improved Donnell's nonlinear shell theory, are developed as

$$(\varepsilon_x^0, \varepsilon_\theta^0, \gamma_{x\theta}^0) = \left(\frac{\partial u}{\partial x} + \frac{1}{2}\left(\frac{\partial w}{\partial x}\right)^2, \frac{1}{R}\left(\frac{\partial v}{\partial \theta} + w\right) + \frac{1}{2}\left(\frac{\partial w}{R\partial \theta}\right)^2, \frac{\partial v}{\partial x} + \frac{1}{R}\frac{\partial u}{\partial \theta} + \frac{1}{R}\frac{\partial w}{\partial \theta}\frac{\partial w}{\partial x}\right), \tag{14}$$

$$(k_x, k_\theta, k_{x\theta}) = \left(-\frac{\partial^2 w}{\partial x^2}, -\frac{1}{R^2}\left(\frac{\partial^2 w}{\partial \theta^2} - \frac{\partial v}{\partial \theta}\right), -\frac{1}{R}\left(\frac{\partial^2 w}{\partial x \partial \theta} - \frac{\partial v}{\partial x}\right)\right). \tag{15}$$

The stress-strain relations are

$$\begin{pmatrix} \sigma_{xx} \\ \sigma_{\theta\theta} \\ \sigma_{x\theta} \end{pmatrix} = \begin{pmatrix} C_{11} & C_{12} & 0 \\ C_{21} & C_{22} & 0 \\ 0 & 0 & C_{66} \end{pmatrix} \begin{pmatrix} \varepsilon_{xx} \\ \varepsilon_{\theta\theta} \\ \gamma_{x\theta} \end{pmatrix}, \tag{16}$$

where $C_{11} = C_{22} = E(z)/(1 - \nu^2)$, $C_{12} = C_{21} = E(z)\nu/(1 - \nu^2)$, and $C_{66} = G(z)$.

The strain energy U_{s1} of the embedded sandwich FG porous thin shell is

$$U_{\text{s1}} = \frac{1}{2} \int_s \int_{-h/2}^{h/2} (\sigma_{xx}\varepsilon_{xx} + \sigma_{\theta\theta}\varepsilon_{\theta\theta} + \sigma_{x\theta}\gamma_{x\theta})\mathrm{d}z\mathrm{d}S$$

$$= \frac{1}{2} \int_s (N_x\varepsilon_x^0 + N_\theta\varepsilon_\theta^0 + N_{x\theta}\gamma_{x\theta}^0 + M_x k_x + M_\theta k_\theta + M_{x\theta}k_{x\theta})\mathrm{d}S. \tag{17}$$

The forces and moments are given by

$$\begin{pmatrix} N_{xx} \\ N_{x\theta} \\ N_{\theta\theta} \end{pmatrix} = \int_{-h/2}^{-h_\text{c}/2} \begin{pmatrix} \sigma_{xx} \\ \sigma_{x\theta} \\ \sigma_{\theta\theta} \end{pmatrix} \mathrm{d}z + \int_{-h_\text{c}/2}^{h_\text{c}/2} \begin{pmatrix} \sigma_{xx} \\ \sigma_{x\theta} \\ \sigma_{\theta\theta} \end{pmatrix} \mathrm{d}z + \int_{h_\text{c}/2}^{h/2} \begin{pmatrix} \sigma_{xx} \\ \sigma_{x\theta} \\ \sigma_{\theta\theta} \end{pmatrix} \mathrm{d}z, \tag{18}$$

$$\begin{pmatrix} M_{xx} \\ M_{x\theta} \\ M_{\theta\theta} \end{pmatrix} = \int_{-h/2}^{-h_\text{c}/2} \begin{pmatrix} \sigma_{xx} \\ \sigma_{x\theta} \\ \sigma_{\theta\theta} \end{pmatrix} z\mathrm{d}z + \int_{-h_\text{c}/2}^{h_\text{c}/2} \begin{pmatrix} \sigma_{xx} \\ \sigma_{x\theta} \\ \sigma_{\theta\theta} \end{pmatrix} z\mathrm{d}z + \int_{h_\text{c}/2}^{h/2} \begin{pmatrix} \sigma_{xx} \\ \sigma_{x\theta} \\ \sigma_{\theta\theta} \end{pmatrix} z\mathrm{d}z. \tag{19}$$

The strain energy U_{s2} induced by elastic media can be defined as

$$U_{\text{s2}} = \frac{1}{2} \int_s k_\text{w} w^2 + k_\text{p}\Big(\Big(\frac{\partial w}{\partial x}\Big)^2 + \Big(\frac{\partial w}{R\partial\theta}\Big)^2\Big)\mathrm{d}S. \tag{20}$$

The kinetic energy of embedded sandwich FG porous shell is

$$T = \frac{1}{2} \int_s I_0\Big(\Big(\frac{\partial u}{\partial t}\Big)^2 + \Big(\frac{\partial v}{\partial t}\Big)^2 + \Big(\frac{\partial w}{\partial t}\Big)^2\Big)\mathrm{d}S, \tag{21}$$

where $I_0 = \int_{-h/2}^{h/2} \rho(z)\mathrm{d}z$.

The transverse external excitation is

$$F(x, \theta, t) = f\cos(\Omega t)\delta(x - x_0)\delta(\theta - \theta_0), \tag{22}$$

in which f denotes the excitation amplitude; Ω is the circular excitation frequency; δ is the Dirac delta function; and (x_0, θ_0) denotes the location of the excitation.

The work performed by external excitation F can be given by

$$W_F = \int_s Fw\mathrm{d}S. \tag{23}$$

By using Hamilton's principle

$$\delta \int_0^t (U_{\text{s1}} + U_{\text{s2}} - T - W_F)\mathrm{d}t = 0, \tag{24}$$

and applying Eqs. (17), (20), (21) and (23) in Eq. (24), the equations of motion for the embedded sandwich FG porous shell can be obtained as follows:

$$\frac{\partial N_x}{\partial x} + \frac{\partial N_{x\theta}}{R\partial\theta} = I_0\frac{\partial^2 u}{\partial t^2}, \tag{25}$$

$$\frac{\partial N_{x\theta}}{\partial x} + \frac{1}{R}\frac{\partial N_\theta}{\partial\theta} + \frac{2}{R}\frac{\partial M_{x\theta}}{\partial x} + \frac{1}{R^2}\frac{\partial M_\theta}{\partial\theta} = I_0\frac{\partial^2 v}{\partial t^2}, \tag{26}$$

$$-\frac{N_\theta}{R} + \frac{1}{R^2}\frac{\partial N_\theta}{\partial\theta}\frac{\partial w}{\partial\theta} + \frac{1}{R^2}\frac{\partial^2 M_\theta}{\partial\theta^2} + \frac{N_\theta}{R^2}\frac{\partial^2 w}{\partial\theta^2} + \frac{\partial N_{x\theta}}{\partial x}\frac{\partial w}{R\partial\theta}$$

$$+ \frac{\partial N_{x\theta}}{R\partial\theta}\frac{\partial w}{\partial x} + \frac{\partial N_x}{\partial x}\frac{\partial w}{\partial x} + 2\frac{\partial^2 M_{x\theta}}{R\partial x\partial\theta} + 2N_{x\theta}\frac{\partial^2 w}{R\partial x\partial\theta} + \frac{\partial^2 M_x}{\partial x^2}$$

$$+ N_x\frac{\partial^2 w}{\partial x^2} - k_\text{w}w + k_\text{p}\Big(\frac{\partial^2 w}{\partial x^2} + \frac{\partial^2 w}{R^2\partial\theta^2}\Big) - ch\frac{\partial w}{\partial t} = I_0\frac{\partial^2 w}{\partial t^2} - F(t), \tag{27}$$

where c is the structure damping coefficient.

The simply supported boundary conditions are

$$v = w = N_x = M_x = 0. \tag{28}$$

3   Solution method

By defining resonant mode with half-wave m and circumference wave n as mode (m, n) for simplicity, an excitation in the neighborhood of resonant mode $(1, n)$ is considered here. The following three displacements are expanded by trigonometric series, which satisfy the boundary conditions[21],

$$u(x, \theta, t) = (UA_{1,n}(t) \cos(n\theta) + UB_{1,n}(t) \sin(n\theta)) \cos(\lambda_1 x), \tag{29}$$

$$
\begin{aligned}
v(x, \theta, t) = &(VA_{1,n}(t) \sin(n\theta) + VB_{1,n}(t) \cos(n\theta)) \sin(\lambda_1 x) \\
&+ (VA_{1,2n}(t) \sin(n\theta) + VB_{1,2n}(t) \cos(n\theta)) \sin(\lambda_1 x) \\
&+ (VA_{3,2n}(t) \sin(n\theta) + VB_{3,2n}(t) \cos(n\theta)) \sin(\lambda_1 x),
\end{aligned} \tag{30}
$$

$$w(x, \theta, t) = (WA_{1,n}(t) \cos(n\theta) + WB_{1,n}(t) \sin(n\theta)) \sin(\lambda_1 x), \tag{31}$$

where $\lambda_1 = m\pi/L$; $UA_{1,n}$, $UB_{1,n}$, $VA_{1,in}$, $VB_{1,in}$, $VA_{3,2n}$, $VB_{3,2n}$, $WA_{1,n}$, and $WB_{1,n}$ ($i = 1, 2$) are displacement amplitude components. The expansion has ten degrees of freedom, which can ensure good accuracy in the calculation performed here. The accuracy of the solution is verified by numerical calculation.

Substituting Eqs. (29)–(31) into Eqs. (25)–(27) and ignoring the effect of inertia in the in-plane direction, and subsequently applying the Galerkin's method[22–25], the ordinary differential equations for the variables $WA_{1,n}$ and $WB_{1,n}$ can be obtained,

$$
\begin{cases}
\ddot{W}A_{1,n}(t) + 2\kappa_1\omega_1\dot{W}A_{1,n}(t) + \omega_1^2 WA_{1,n}(t) + a_1 WA_{1,n}^3(t) + a_2 WA_{1,n}(t)WB_{1,n}^2(t) \\
= \dfrac{f}{I_{10}}\cos(\Omega t), \\
\ddot{W}B_{1,n}(t) + 2\kappa_2\omega_2\dot{W}B_{1,n}(t) + \omega_2^2 WB_{1,n}(t) + a_3 WB_{1,n}^3(t) \\
+ a_4 WA_{1,n}^2(t)WB_{1,n}(t) = 0,
\end{cases} \tag{32}
$$

where κ_1, κ_2, a_1, a_2, a_3, and a_4 denote constant coefficients.

Then, the multiple scales method[26–27] is employed to solve Eq. (32). First, the scaled time is assumed in the form

$$T_n = \varepsilon^n t, \quad n = 0, 1, 2, \cdots, \tag{33}$$

in which ε denotes a small dimensionless parameter.

The time derivatives in terms of T_n become

$$
\begin{cases}
\dfrac{\partial}{\partial t} = \dfrac{\partial}{\partial T_0} + \varepsilon\dfrac{\partial}{\partial T_1} + \varepsilon^2\dfrac{\partial}{\partial T_2} + \cdots = D_0 + \varepsilon D_1 + \varepsilon^2 D_2 + \cdots, \\
\dfrac{\partial^2}{\partial t^2} = \dfrac{\partial}{\partial t}\Big(\dfrac{\partial}{\partial T_0} + \varepsilon\dfrac{\partial}{\partial T_1} + \varepsilon^2\dfrac{\partial}{\partial T_2} + \cdots\Big) = D_0^2 + 2\varepsilon D_0 D_1 + \varepsilon^2(D_1^2 + 2D_0 D_2) + \cdots,
\end{cases} \tag{34}
$$

in which D_n is defined as

$$D_n = \dfrac{\partial}{\partial T_n}, \quad n = 0, 1, 2, \cdots. \tag{35}$$

The response, which is the function of different scaled times, can be written as follows:

$$\begin{cases} WA_{1,n} = \varepsilon WA_{11}(T_0, T_2) + \varepsilon^3 WA_{13}(T_0, T_2), \\ WB_{1,n} = \varepsilon WB_{11}(T_0, T_2) + \varepsilon^3 WB_{13}(T_0, T_2). \end{cases} \tag{36}$$

By inserting Eq. (36) into Eq. (32), and defining $\kappa_i = \varepsilon^2 \kappa_{i0}$ and $f/I_{10} = \varepsilon^3 f_{1,n}$, we get

$$\begin{cases} \varepsilon(D_0^2 WA_{11}(T_0, T_2) + \omega_1^2 WA_{11}(T_0, T_2)) = 0, \\ \varepsilon(D_0^2 WB_{11}(T_0, T_2) + \omega_2^2 WB_{11}(T_0, T_2)) = 0, \end{cases} \tag{37}$$

and

$$\begin{cases} \varepsilon^3\big(-f_{1,n}\cos(T_0\Omega) + a_1 WA_{11}^3(T_0, T_2) + \omega_1^2 WA_{13}(T_0, T_2) \\ \quad + a_2 WA_{11}(T_0, T_2)WB_{11}^2(T_0, T_2) + 2\xi_{10}\omega_1 D_0 WA_{11}(T_0, T_2) \\ \quad + 2D_0 D_2 WA_{11}(T_0, T_2) + D_0^2 WA_{13}(T_0, T_2)\big) = 0, \\ \varepsilon^3\big(a_4 WA_{11}^2(T_0, T_2)WB_{11}(T_0, T_2) + a_3 WB_{11}^3(T_0, T_2) + \omega_2^2 WB_{13}(T_0, T_2) \\ \quad + 2\xi_{20}\omega_2 D_0 WB_{11}(T_0, T_2) + 2D_0 D_2 WB_{11}(T_0, T_2) + D_0^2 WB_{13}(T_0, T_2)\big) = 0. \end{cases} \tag{38}$$

The solution to Eq. (39) could be assumed in the form

$$\begin{cases} WA_{11}(T_0, T_2) = \Lambda_1(T_2)e^{i\omega_1 T_0} + \overline{\Lambda}_1(T_2)e^{-i\omega_1 T_0}, \\ WB_{11}(T_0, T_2) = \Lambda_2(T_2)e^{i\omega_2 T_0} + \overline{\Lambda}_2(T_2)e^{-i\omega_2 T_0}, \end{cases} \tag{39}$$

where $\overline{\Lambda}_1$ and $\overline{\Lambda}_2$ denote the conjugate functions of Λ_1 and Λ_2, respectively. Due to the resonance of the system occurs at $\Omega \approx \omega_1$ and $\omega_1 \approx \omega_2$, two detuning parameters σ_1 and σ_2 are used to measure the frequency distance, which can be written as follows:

$$\Omega = \omega_1 + \varepsilon^2 \sigma_1, \quad \omega_1 = \omega_2 + \varepsilon^2 \sigma_2. \tag{40}$$

Substituting Eqs. (39)–(40) into Eq. (38) and letting the coefficients of the secular terms equal to zero yield

$$\begin{cases} \Big(-\dfrac{1}{2}e^{iT_2\sigma_1}f_{1,n} + 2i\xi_{10}\omega_1^2\Lambda_1(T_2) + 3a_1\Lambda_1^2(T_2)\overline{\Lambda}_1(T_2) + a_2 e^{-2iT_2\sigma_2}\Lambda_2^2(T_2)\overline{\Lambda}_1(T_2) \\ \quad + 2a_2\Lambda_1(T_2)\Lambda_2(T_2)\overline{\Lambda}_2(T_2) + 2i\omega_1 D_2\Lambda_1(T_2)\Big) = 0, \\ \big(2i\xi_{20}\omega_2^2\Lambda_2(T_2) + 2a_4\Lambda_1(T_2)\Lambda_2(T_2)\overline{\Lambda}_1(T_2) + a_4 e^{2iT_2\sigma_2}\Lambda_1^2(T_2)\overline{\Lambda}_2(T_2) \\ \quad + 3a_3\Lambda_2^2(T_2)\overline{\Lambda}_2(T_2) + 2i\omega_2 D_2\Lambda_2(T_2)\big) = 0. \end{cases} \tag{41}$$

To write the modulation equations in polar coordinates, the amplitude functions are set as

$$\Lambda_1(T_2) = \frac{1}{2}b_1 e^{i\theta_1}, \quad \Lambda_2(T_2) = \frac{1}{2}b_2 e^{i\theta_2}, \tag{42}$$

in which b_j and θ_j denote the real numbers of T_2. Substituting Eq. (42) into Eq. (41) and separating the real and imaginary parts yield

$$\begin{cases} 3a_1 b_1^3 + 2a_2 b_1 b_2^2 - 4f_{1,n}\cos\gamma_1 + a_2 b_1 b_2^2\cos\gamma_2 - 8\omega_1 b_1 \theta_1' = 0, \\ 8i\xi_{10}\omega_1^2 b_1 - 4if_{1,n}\sin\gamma_1 - ia_2 b_1 b_2^2\sin\gamma_2 + 8i\omega_1 b_1' = 0, \\ 2a_4 b_1^2 b_2 + 3a_3 b_2^3 + a_4 b_1^2 b_2\cos\gamma_2 - 8\omega_2 b_2 \theta_2' = 0, \\ 8i\xi_{20}\omega_2^2 b_2 + ia_4 b_1^2 b_2\sin\gamma_2 + 8i\omega_2 b_2' = 0, \end{cases} \tag{43}$$

where

$$\gamma_1 = T_2\sigma_1 - \theta_1, \quad \gamma_2 = 2T_2\sigma_2 + 2\theta_1 - 2\theta_2. \tag{44}$$

The frequency response equations, by utilizing $b'_j = \gamma'_j = 0$ ($j = 1, 2$), can be obtained as

$$\begin{cases} 3a_1b_1^3 + 2a_2b_1b_2^2 - 4f_{1,n}\cos\gamma_1 + a_2b_1b_2^2\cos\gamma_2 - 8\omega_1b_1\sigma_1 = 0, \\ 8\mathrm{i}\xi_{10}\omega_1^2b_1 - 4\mathrm{i}f_{1,n}\sin\gamma_1 - \mathrm{i}a_2b_1b_2^2\sin\gamma_2 = 0, \\ 2a_4b_1^2b_2 + 3a_3b_2^3 + a_4b_1^2b_2\cos\gamma_2 - 8\omega_2b_2(\sigma_1 + \sigma_2) = 0, \\ 8\mathrm{i}\xi_{20}\omega_2^2b_2 + \mathrm{i}a_4b_1^2b_2\sin\gamma_2 = 0. \end{cases} \tag{45}$$

The stability of the system could be determined by the eigenvalues of the Jacobian matrix of Eq. (45).

4 Results and discussion

4.1 Validation

To verify the correctness of derivation, the natural frequencies of an isotropic thin shell available in literature and those obtained in the present study are compared initially as listed in Table 1. The results show good agreement, where the small difference might be mainly caused by the different shell theories.

Table 1 Comparison of natural frequencies ω_{mn} of isotropic thin shell with simply supported boundary conditions ($E = 71.02 \times 10^9$ N/m^2, $\nu = 0.31$, $\rho = 2\,796$ kg/m^3, $h = 0.247 \times 10^{-3}$ m, $R = 0.1$ m, and $L = 0.2$ m)

(m, n)	Qin et al.[28]	Present
(1, 5)	722.1	737.83
(1, 6)	553.3	561.57
(1, 7)	484.6	489.78
(1, 8)	489.6	493.56
(1, 9)	546.2	549.70
(1, 10)	636.8	640.10
(1, 11)	750.7	753.85
(1, 12)	882.2	885.37

Considering that there is no appropriate result from literature on internal resonance of isotropic thin shells for comparison studies, the present results are compared with numerical results via the Pseudo-arclength continuation method on the platform of MATLAB[29]. By adopting the material and geometrical parameters listed in Table 1, the nonlinear resonant responses of thin cylindrical shell are calculated, where the external excitation amplitude is $f_{1,n} = 0.000\,2h\omega_{1,n}^2$, the location of the excitation is $x_0 = L/2$, $\theta_0 = 0$, the damping ratio is $2\kappa_i = 0.001$, $k_{\mathrm{w}} = k_{\mathrm{p}} = 0$, and $\varepsilon = 0.01$. The mode (1, 7) is considered here. Owing to the axial symmetry of the shell, there are two conjugate modes with $n = 7$ associated with the same natural frequency, that is, one described by $\cos(7\theta)$ and the other by $\sin(7\theta)$. Hence, there exists a 1:1 internal resonance between the two conjugate modes. A comparison of the frequency-response curve is shown in Fig. 3. One can see that the present results match those obtained via the numerical method very well, bespeaking the validity of the present study.

4.2 Results of embedded sandwich FG porous shell

In what follows, the nonlinear dynamics analysis of an embedded sandwich FG porous shell is investigated, and the following parameters, if not specified, are considered as $E = 200$ GPa, $\rho = 7\,850$ kg/m^3, $\nu = 0.33$, $h_{\mathrm{f}} = 0.247 \times 10^{-4}$ m, $h_{\mathrm{c}} = 8h_{\mathrm{f}}$, $L = 0.2$ m, $R = 0.5L$, $\zeta_0 = 0.2$,
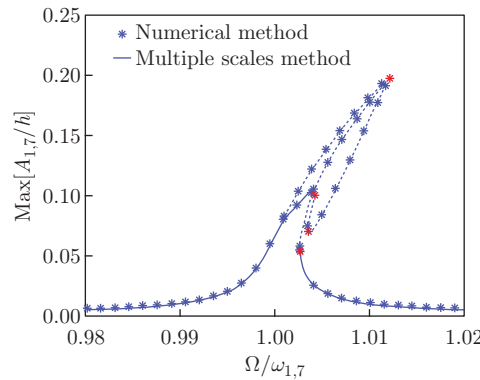
Fig. 3 Comparison of frequency-response curve of thin cylindrical shell (dotted line: unstable analytical solution; solid line: stable analytical solution) (color online)

$k_{\mathrm{w}} = k_{\mathrm{p}} = 0$, $f_{1,n} = 0.000\ 2h\omega_{1,n}^2$, $x_0 = L/2$, $\theta_0 = 0$, $2\kappa_i = 0.001$, and $\varepsilon = 0.01$. The mode $(1,7)$ is considered here, which corresponds to the fundamental frequency.

The effect of external excitation on frequency-response curves of the embedded sandwich FG porous shell with porous metal foam-I distribution is presented in Fig. 4, where the dashed and solid lines are the unstable and stable analytical solutions, respectively. The response magnitude of the driven mode is about twice that of the companion mode. Additionally, one can find that the system exhibits hardening-spring behavior. With the increase in the excitation frequency from low level to high level, the coupled response loses its stability via a bifurcation. Furthermore, as the amplitude of external excitation increases, the response magnitude increases obviously. Meanwhile, the coupled interaction between driven and companion modes becomes more and more evident at the same time.
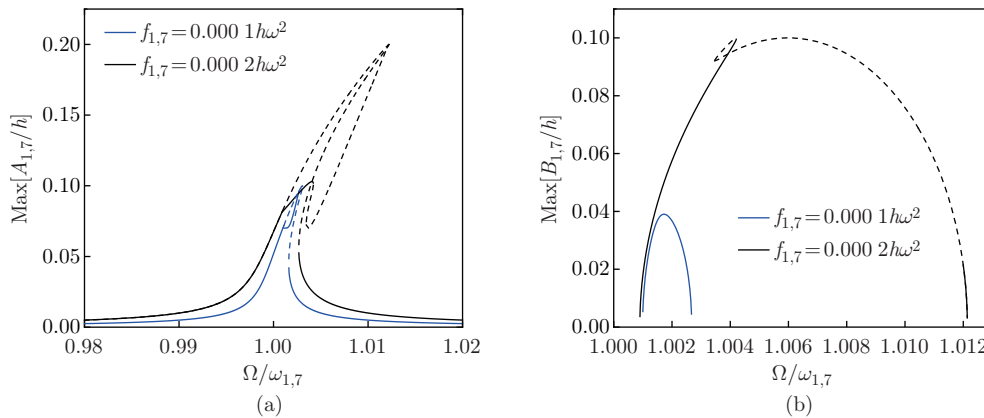

(a)

(b)

Fig. 4 Effect of external excitation on frequency-response curves: (a) maximum of $A_{1,7}/h$; (b) maximum of $B_{1,7}/h$ (dotted line: unstable analytical solution; solid line: stable analytical solution) (color online)

Figure 5 shows the effect of porous metal foam distribution type on the frequency-response curves of the embedded sandwich FG porous shell. It is noted that the embedded sandwich FG shell with porous metal foam distribution-II has the most evident hardening-spring behavior, while the porous metal foam-I shell has the weakest one. Besides, the resonant amplitude of the embedded sandwich FG porous shell changes slightly when the porous metal foam distribution

type alters, indicating the porous metal foam distribution type has insignificant effect on the vibration amplitude of the system.
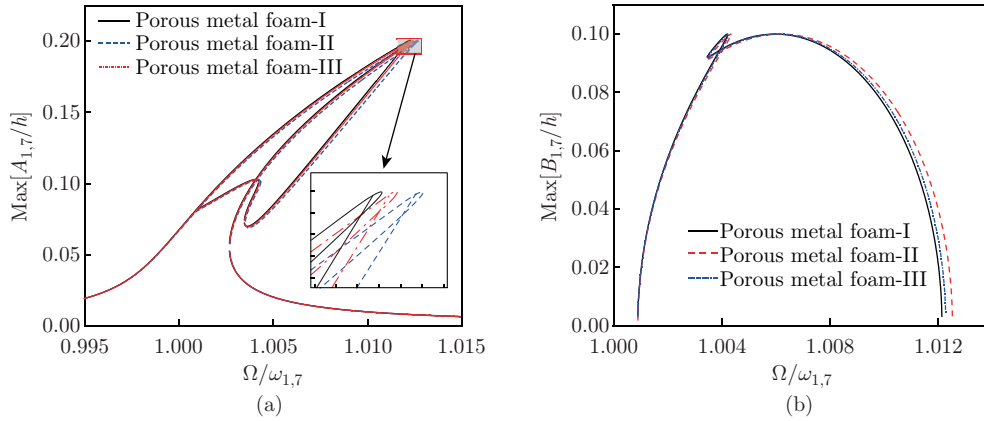

Fig. 5 Effect of porous metal foam distribution type on frequency-response curves: (a) maximum of $A_{1,7}/h$; (b) maximum of $B_{1,7}/h$ (color online)

The frequency-response curves of the embedded sandwich FG porous shell under different foam coefficients are shown in Fig. 6. Four cases of foam coefficient $\zeta_0 = 0$, $\zeta_0 = 0.2$, $\zeta_0 = 0.4$, and $\zeta_0 = 0.6$ are considered. As can be seen, the resonance domain of the system moves to the low frequency ratio region with the increase in the foam coefficient; in fact, the large foam coefficient could decrease the natural frequencies of the system. In addition, with the increase in the foam coefficient, the hardening-spring behavior of the system becomes weaker and weaker.
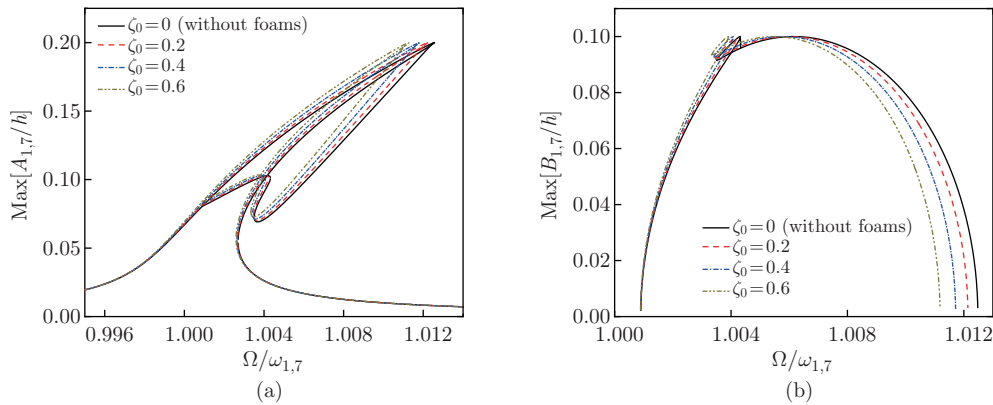

Fig. 6 Effect of foam coefficient on frequency-response curves: (a) maximum of $A_{1,7}/h$; (b) maximum of $B_{1,7}/h$ (porous metal foam-I) (color online)

In order to discuss the role of elastic foundations in the dynamic behaviors more clearly, Figs. 7–8 show the effect of Winkler and Pasternak foundation parameters on the frequency-response curves of the embedded sandwich FG porous shell. It can be found that an increase in Winkler or Pasternak foundation parameters results in the weakening of the hardening-spring characteristics of the system. For driven and companion modes, the resonance domain narrows as the Winkler or Pasternak foundation parameters increase. Furthermore, it is clear that the hardening nonlinearity behavior of system with Pasternak foundation parameter is less than the Winkler foundation parameter.
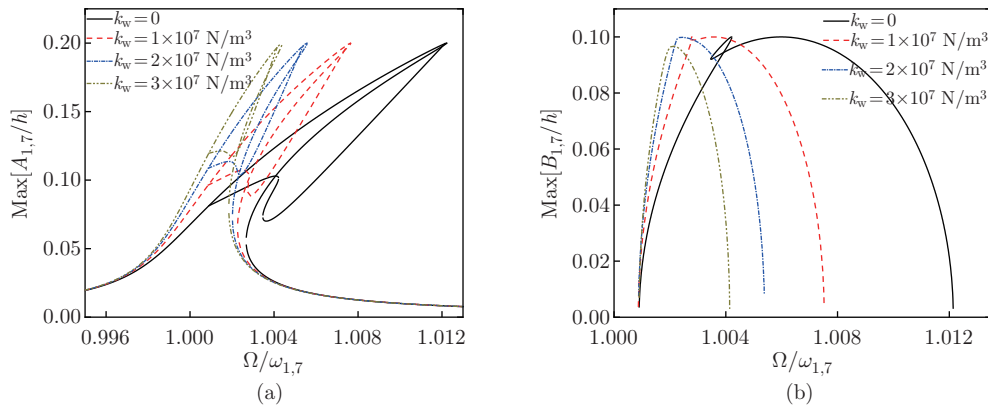
Fig. 7 Effect of Winkler foundation parameter on frequency-response curves: (a) maximum of $A_{1,7}/h$; (b) maximum of $B_{1,7}/h$ (porous metal foam-I) (color online)
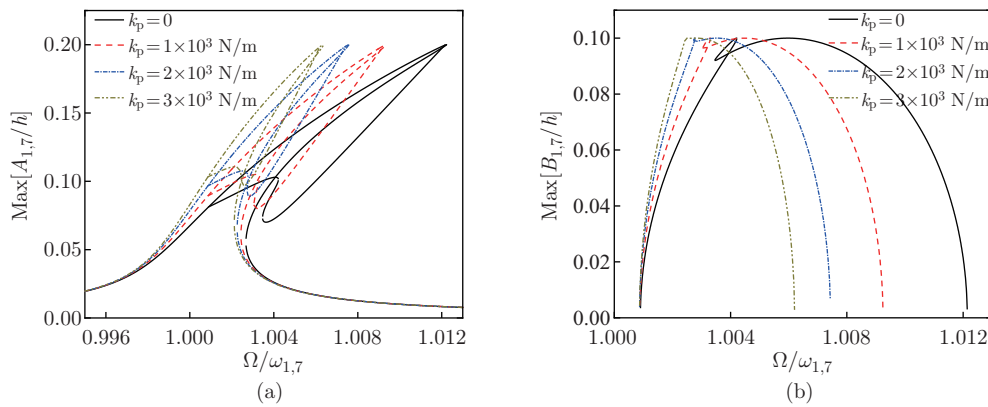

Fig. 8 Effect of Pasternak foundation parameter on frequency-response curves: (a) maximum of $A_{1,7}/h$; (b) maximum of $B_{1,7}/h$ (porous metal foam-I) (color online)

Figure 9 highlights the effect of damping ratio on the frequency-response curves of the embedded sandwich FG porous shell. As expected, the embedded sandwich FG shell with a smaller damping ratio has a larger resonant amplitude, since the damping ratio reduces the dynamic response of the embedded sandwich FG porous shell.

The effect of core-to-face ratio on the frequency-response curves of embedded sandwich FG porous shell is plotted in Fig. 10. Examining the figure shows that a larger core-to-face ratio makes the resonance domain of both modes move towards the direction of high frequency ratio, which indicates that an increasing core-to-face ratio could generate more notable hardening-spring behavior of the system. At a given excitation frequency ratio, the increase in the core-to-face ratio reduces the response magnitude of the embedded sandwich FG porous shell.

Figure 11 gives the effect of radius-to-length ratio on the frequency-response curves of the embedded sandwich FG porous shell. In this case, one can find that an increase in radius-to-length ratio weakens the hardening-spring behavior. For driven and companion modes, the resonance domains narrow as the radius-to-length ratio increases.

5 Conclusions

In this paper, the nonlinear internal resonance of sandwich FG porous cylindrical shells embedded in elastic media is investigated, where three types of porosity distribution are considered. The governing equations are derived by using the improved Donnell's nonlinear shell
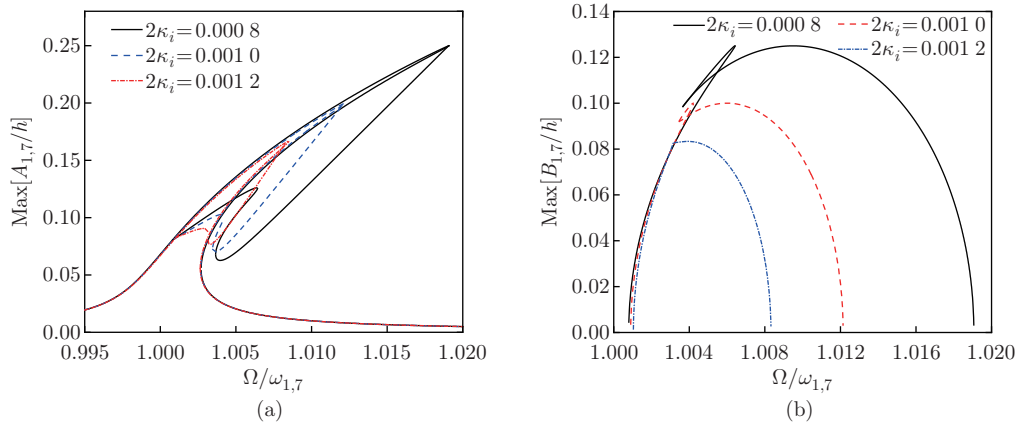
Fig. 9 Effect of damping ratio on frequency-response curves: (a) maximum of $A_{1,7}/h$; (b) maximum of $B_{1,7}/h$ (Porous metal foam-I) (color online)
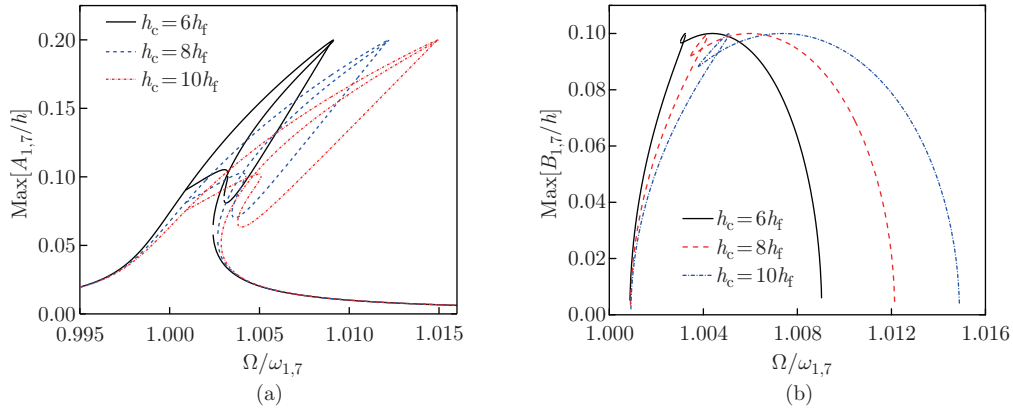

Fig. 10 Effect of core-to-face ratio on frequency-response curves: (a) maximum of $A_{1,7}/h$; (b) maximum of $B_{1,7}/h$ (porous metal foam-I) (color online)
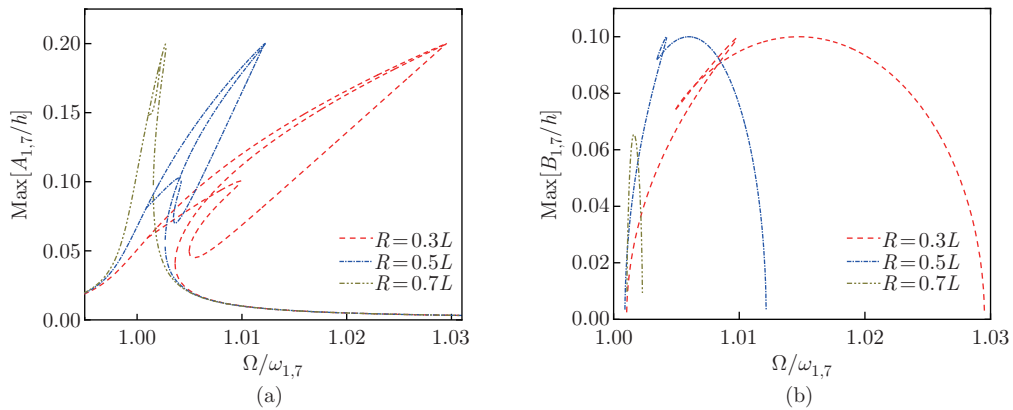

Fig. 11 Effect of radius-to-length ratio on frequency-response curves: (a) maximum of $A_{1,7}/h$; (b) maximum of $B_{1,7}/h$ (porous metal foam-I) (color online)

theory and Hamilton's principle, and then transformed into a set of ordinary differential equations through the Galerkin method. Afterwards, an approximate analytical solution is obtained by means of the multiple scales method. Finally, parametric studies of embedded sandwich FG metal foam porous shells are conducted in detail. Main highlights and conclusions are stated as follows.

An improved nonlinear displacement expansion method, which requires no Airy stress function, is adopted to solve the nonlinear forced vibrations of the present shells. Compared with the traditional nonlinear governing equations including the Airy stress function, the difficulty of solving the nonlinear vibration issue of thin shells is reduced effectively. The correctness of the method is proved by the numerical verification.

The nonlinear tendency of the system exhibits hardening-spring behavior. The response magnitude of the driven mode is about twice that of the companion mode. The embedded sandwich FG shell with porous metal foam distribution-II has the most evident hardening-spring behavior, while the porous metal foam-I shell has the weakest one. In addition, enlarging the core-to-face ratio yields more notable hardening-spring behavior of the system. Higher values for foam coefficient and Winkler/Pasternak foundation parameters correspond to the weakening of the hardening-spring behavior of the embedded sandwich FG porous thin shell.

References

[1] SPOERKE, E. D., MURRAY, N. G., LI, H., BRINSON, L. C., and STUPP, S. I. A bioactive titanium foam scaffold for bone repair. *Acta Biomaterialia*, **1**, 523–533 (2005)

[2] CAO, L., LIN, Y., LU, F., CHEN, R., ZHANG, Z., and LI, Y. Experimental study on the shock absorption performance of combined aluminium honeycombs under impact loading. *Shock and Vibration*, **2015**, 1–8 (2015)

[3] LI, M., DENG, Z., LIU, R., and GUO, H. Crashworthiness design optimisation of metal honeycomb energy absorber used in lunar lander. *International Journal of Crashworthiness*, **16**, 411–419 (2011)

[4] TAN, W. C., SAW, L. H., XUAN, H. S., CAI, Z., and THIAM,M .C. Overview of porous media/metal foam application in fuel cells and solar power systems. *Renewable and Sustainable Energy Reviews*, **96**, 181–197 (2018)

[5] CHOI, K., KIM, J., KO, A., MYUNG, C. L., PARK, S., and LEE, J. Size-resolved engine exhaust aerosol characteristics in a metal foam particulate filter for GDI light-duty vehicle. *Journal of Aerosol science*, **57**, 1–13 (2013)

[6] KIM, S. and LEE, C. W. A review on manufacturing and application of open-cell metal foam. *Procedia Materials Science*, **4**, 305–309 (2014)

[7] BRESLAVSKY, I. D. and AMABILI, M. Nonlinear vibrations of a circular cylindrical shell with multiple internal resonances under multi-harmonic excitation. *Nonlinear Dynamics*, **93**, 53–62 (2018)

[8] YANG, S. W., ZHANG, W., and MAO, J. J. Nonlinear vibrations of carbon fiber reinforced polymer laminated cylindrical shell under non-normal boundary conditions with 1: 2 internal resonance. *European Journal of Mechanics-A/Solids*, **74**, 317–336 (2019)

[9] ZHANG, Y., LIU, J., and WEN, B. Nonlinear dynamical responses of rotary cylindrical shells with internal resonance. *Acta Mechanica Solida Sinica*, **32**, 186–200 (2019)

[10] RODRIGUES, L., SILVA, F. M. A., and GONÇALVES, P. B. Influence of initial geometric imperfections on the 1:1:1:1 internal resonances and nonlinear vibrations of thin-walled cylindrical shells. *Thin-Walled Structures*, **151**, 106730 (2020)

[11] LIU, Y., QIN, Z. Y., and CHU, F. L. Analytical study of the impact response of shear deformable sandwich cylindrical shell with a functionally graded porous core. *Mechanics of Advanced Materials and Structures*, **5**, 1–10 (2020)

[12] DONG, Y. H., LI, Y. H., CHEN, D., and YANG, J. Vibration characteristics of functionally graded graphene reinforced porous nanocomposite cylindrical shells with spinning motion. *Composites Part B*: *Engineering*, **145**, 1–13 (2018)

[13] LI, Q., DI, W., CHEN, X., LEI, L., YU, Y., and WEI, G. Nonlinear vibration and dynamic buckling analyses of sandwich functionally graded porous plate with graphene platelet reinforcement resting on Winkler-Pasternak elastic foundation. *International Journal of Mechanical Sciences*, **148**, 596–610 (2018)

[14] CHEN, D., YANG, J., and KITIPORNCHAI, S. Free and forced vibrations of shear deformable functionally graded porous beams. *International Journal of Mechanical Sciences*, **108-109**, 14–22 (2016)

[15] GAO, W., QIN, Z., and CHU, F. Wave propagation in functionally graded porous plates reinforced with graphene platelets. *Aerospace Science and Technology*, **102**, 105860 (2020)

[16] LIU, Y. F. and WANG, Y. Q. Thermo-electro-mechanical vibrations of porous functionally graded piezoelectric nanoshells. *Nanomaterials*, **9**, 301 (2019)

[17] MAGNUCKI, K. and STASIEWICZ, P. Elastic buckling of a porous beam. *Journal of Theoretical and Applied Mechanics*, **42**, 859–868 (2004)

[18] MAGNUCKA-BLANDZI, E. Axi-symmetrical deflection and buckling of circular porous-cellular plate. *Thin-Walled Structures*, **46**, 333–337 (2008)

[19] JABBARI, M., MOJAHEDIN, A., KHORSHIDVAND, A. R., and ESLAMI, M. R. Buckling analysis of a functionally graded thin circular plate made of saturated porous materials. *Journal of Engineering Mechanics*, **140**, 287–295 (2013)

[20] CHEN, D., YANG, J., and KITIPORNCHAI, S. Elastic buckling and static bending of shear deformable functionally graded porous beam. *Composite Structures*, **133**, 54–61 (2015)

[21] AMABILI, M. *Nonlinear Vibrations and Stability of Shells and Plates*, Cambridge University Press, Cambridge (2008)

[22] DING, H., HUANG, L., MAO, X., and CHEN, L. Primary resonance of traveling viscoelastic beam under internal resonance. *Applied Mathematics and Mechanics* (*English Edition*), **38**, 1–14 (2017) https://doi.org/10.1007/s10483-016-2152-6

[23] LI, W., YANG, X. D., ZHANG, W., and REN, Y. Parametric amplification performance analysis of a vibrating beam micro-gyroscope with size-dependent and fringing field effects. *Applied Mathematical Modelling*, **91**, 111–124 (2021)

[24] LIU, Y. F., LING, X., and WANG, Y. Q. Free and forced vibration analysis of 3D graphene foam truncated conical microshells. *Journal of the Brazilian Society of Mechanical Sciences and Engineering*, **43**, 133 (2021)

[25] WANG, Y., LIU, Y., and ZU, J. W. Nonlinear free vibration of piezoelectric cylindrical nanoshells. *Applied Mathematics and Mechanics* (*English Edition*), **40**, 13–32 (2019) https://doi.org/10.1007/s10483-019-2476-6

[26] NAYFEH, A. H. and MOOK, D. T. *Nonlinear Oscillations*, John Wiley & Sons, New Jersey (1995)

[27] ZHANG, W., CHEN, J., ZHANG, Y. F., and YANG, X. D. Continuous model and nonlinear dynamic responses of circular mesh antenna clamped at one side. *Engineering Structures*, **151**, 115–135 (2017)

[28] QIN, Z., CHU, F., and ZU, J. Free vibrations of cylindrical shells with arbitrary boundary conditions: a comparison study. *International Journal of Mechanical Sciences*, **133**, 91–99 (2017)

[29] DHOOGE, A., GOVAERTS, W., KUZNETSOV, Y. A., MEIJER, H. G. E., and SAUTOIS, B. New features of the software MatCont for bifurcation analysis of dynamical systems. *Mathematical and Computer Modelling of Dynamical Systems*, **14**, 147–175 (2008)